

ENHANCEMENT OF LASCO C1, C2, AND C3 CORONAGRAPH IMAGES

NRL Grant N00014-97-1-GO23

Annual Report

For the Period 1 February 1998 through 31 January 1999

Principal Investigator
Dr. Margarita Karovska

January 1999

DISTRIBUTION STATEMENT A

Approved for public release
Distribution Unlimited

Prepared for:

Department of the Navy
Naval Research Laboratory
Washington, D.C. 20375-5326

Smithsonian Institution
Astrophysical Observatory
Cambridge, Massachusetts 02138

The Smithsonian Astrophysical Observatory
is a member of the
Harvard-Smithsonian Center for Astrophysics

19990209 032

The NRL Scientific Officer for this grant is Richard Rubin, Naval Research Laboratory, CODE 7605.10, 4555 Overlook Avenue S.W., Washington, D.C. 20375-5326.

1 Introduction

The Large Angle Spectrometric Coronagraph (LASCO) on board SOHO provided unprecedented views of the solar corona since January 1996. This instrument contains three individual coronagraphs C1, C2, and C3, described in detail in Brueckner et al (1995). The C1 coronagraph acquires high resolution images ($11''$ and higher) of the lower corona from $1.1 R_{\odot}$ to $3.0 R_{\odot}$, thereby providing a close link to the disk observations of other instruments in the SOHO complement. The C2 and C3 images have lower resolution ($23''$ and about $2'$ respectively), however they provide a unique view of the extended corona up to $32 R_{\odot}$.

During the past year we carried out a study of the morphology and dynamical evolution of various structures in the solar corona as observed by LASCO and EIT. In the following, we summarize the results of this studies.

2 Coronal Variability

Early this past year we completed a project in which we used Fe XIV $\lambda 5303$ green line images obtained by the LASCO C1 coronagraph to search for variability in the quiescent solar corona on timescales of minutes (Wood et al. 1998a,b). The observing program obtained images of a small area of the inner corona every two minutes over a period of one hour. We

analyzed two executions of this program taken several months apart. The most obvious variability observed in these two observing sequences is in the form of long term, quasi-steady brightening on timescales of at least an hour. Of particular interest are two loops which are observed to brighten by at least 25% during the course of the observations. In both cases, the brightening is greatest at the apparent loop tops, and in one loop there appears to be a flow up one of the legs of the loop. This loop-top brightening is reminiscent of loop-top brightenings commonly observed in X-rays during solar flares (see, e.g., Acton et al. 1992).

Based on a preliminary intensity calibration of the C1 coronagraph and using available atomic physics calculations, we find that the range of emission measures implied by the observed intensities in these loops is $n_e^2 \Delta L = (0.2 - 2.0) \times 10^{27} \text{ cm}^{-5}$. This is over an order of magnitude lower than typical active region emission measures measured on the disk at the $1.8 \times 10^6 \text{ K}$ formation temperature of Fe XIV $\lambda 5303$ (Dere & Mason 1993). This suggests that densities for our lines of sight may be at least 4 times lower than typical active region densities measured on the disk of about $6 \times 10^9 \text{ cm}^{-3}$ (Dere & Mason 1993), which would not be surprising considering that our measurements are of the solar limb at a height of about $1.2 R_\odot$. Brighter, denser loops lying below heights of $1.1 R_\odot$ do not extend beyond the inner edge of the LASCO C1 occulter, and are therefore not observed.

3 Coronal Mass Ejections (CME)

We have analyzed two CMEs from 1997 April 30 and 1997 February 23 (Wood et al. 1998c; 1999a) that look very much like a 1997 April 13 LASCO CME studied by Chen et al. (1997) which had a particularly well-defined structure. Chen et al. compared the observations of that CME with an MHD model of an expanding flux rope and found the two to be consistent. The CMEs that we studied are clearly detected in all three LASCO coronagraphs (C1, C2, and C3), and in EIT images as well, in contrast to the April 13 CME which was only seen in C2 and C3. Thus, the April 30 and February 23 CMEs allow for a more detailed comparison with the predictions of the flux rope model.

Several C2 images of the April 30 CME are shown in Figure 1. These images are shown both after the background is subtracted using an average-differencing technique (upper panels) and after edge-enhancement (lower panels). The CME on February 23 is accompanied by a dramatic prominence eruption and a significant GOES X-ray flare, while the April 30 CME is accompanied by no apparent prominence eruption and only a weak X-ray flare. In the C2 and C3 fields of view, both CMEs show the same basic structure as the April 13 CME — a circular rim surrounding a relatively dark cavity containing bright material near the trailing edge.

In Figure 1, the locations of the leading edge (plus signs), trailing edge (X's), and sides (asterisks) of the April 30 CME are indicated. These measurements are used to compute the centroids of the CME, which are also shown in the figures (circles). In the top panel of Figure 2, height-vs.-time plots are displayed for the leading edge, centroid, and trailing edge of the April 30 CME.

By taking first derivatives of the height curves, we can derive empirical velocity curves. In order to do this we first perform polynomial fits to the height data and then analytically compute the derivatives. Simple second order polynomials are sufficient to fit the centroid and trailing edge curves. Much higher order polynomials are required to fit the leading edge curves, so rather than fitting a single polynomial to the data, we have instead broken these curves into two pieces and fitted two separate low-order polynomials to them.

The resulting velocity curves are plotted as shaded regions in the bottom panel of Figure 2, where the shading encompasses the 1σ uncertainty boundaries estimated using Monte Carlo techniques. Most of the acceleration of both the April 30 and February 23 CMEs occurs below about $4 R_{\odot}$, after which the velocities level off. The CMEs exhibit different levels of kinetic energy, with the leading edges of the February 23 and April 30 CMEs reaching speeds of about 900 and 300 km s^{-1} , respectively.

We compared the measured kinematic properties of the two CMEs with the predictions of the erupting flux rope model discussed by Chen et al. (1997) and Chen (1996). Both of our CMEs have well-defined circular rims which can be interpreted as marking the outline of the apex of the flux rope as viewed from the side, meaning that the flux rope is assumed to have an east-west orientation.

In the model, the initially stable flux rope is set in motion by an increase in the poloidal component of the flux rope's magnetic field, which is helical in the rope's interior. The C2 observations of the April 30 CME show helical lines below the rim of the CME (see Fig. 1), which suggests the possible presence of a helical magnetic field such as that assumed in the model. The magnetic flux injection profile $d\Phi_p/dt$ is the primary free parameter that we use to match the dynamic characteristics of individual CMEs.

Figure 2 shows our best fit to the observations for the April 30 CME. We define an observable aspect ratio, $\Lambda(t) \equiv R_c(t)/D(t)$, where $R_c(t)$ is the heliocentric height of the centroid and $D(t)$ is the width of the observed circular rim. In the middle panel of Figure 2, the observed and model values of Λ are plotted for the CMEs. Also shown in the middle panels are the normalized injection profiles ($d\Phi_p/dt$) used in the flux rope calculations.

Our theoretical curves are not perfect fits to the data (see Fig. 2), but they are close enough to support the claim that the flux rope model has captured the essential physics of the CME. Thus, we have demonstrated that the flux rope model is capable of matching the dynamics of CMEs at early times as well as late times, and is also capable of modeling CMEs

with very different velocities and accompanying phenomena.

4 Polar Jets

In addition to our studies of CMEs, we have also looked at LASCO and EIT observations of jets observed in the Sun's polar regions. As seen in LASCO's C2 coronagraph, which images the corona from about $2 R_{\odot}$ to $6 R_{\odot}$, the jets appear as narrow, radially extended intensity enhancements that appear to move outwards from the Sun's polar regions in a nearly radial direction (Wang et al. 1998). We focused our study on several jets detected in two sequences of C2 images recorded on 1997 March 22 and on 1997 August 5-6 (Karovska et al. 1999a,b; Wood et al. 1999b).

We selected thin sectors centered on the axis of the jets. These sectors were partitioned into numerous (~ 70) segments. We measured intensities along the axis of each sector by summing the pixels within individual segments. For each intensity tracing, we fitted a Gaussian to the intensity profile to determine the location of the centroid of the jet. In Figure 3 we plot these centroids for three jets from 1997 August 5. These particular jets are detected in single EIT images as well, which provide us with the first data points shown in Figure 3.

The first few data points of each of the curves in Figure 3 suggest a deceleration of the jets. The simplest possible interpretation for the deceleration seen for the polar jets is that it is due to gravity. In order to test this interpretation, we have fitted the centroid data points in Figure 3 with ballistic trajectory curves. However, there are statistically significant discrepancies between the fits and the data, the largest of which are seen for the jet in Figure 3c. These discrepancies suggest gravity may not be the only force acting on the jets.

The initial velocities of the fitted ballistic trajectories provide another argument against purely ballistic motion. All of the ballistic trajectory fits to the 1997 March and 1997 August jets suggest initial velocities in a narrow range of $540\text{--}590 \text{ km s}^{-1}$. Wang et al. (1998) also noted the rather homogeneous kinematic behavior of the LASCO polar jets. In the gravitational deceleration scenario, jets with initial velocities below about 500 km s^{-1} will never reach the C2 field of view, so explaining the lower initial velocity limit is not a problem. The upper limit, however, is not easy to explain. If the impulsive acceleration followed by gravitational deceleration scenario is true, why are there no jets with initial velocities greater than 610 km s^{-1} and velocities in the C2 field of view greater than 300 km s^{-1} ?

One possibility is that within the C2 field of view the jets may have been incorporated into the ambient solar wind flow. If the polar jets are just following the general wind outflow,

they can be used as tracers for this wind. This could be extremely useful for detailed studies of the solar wind in coronal holes.

5 Future Plans

We plan to continue our study of the kinematic properties of CMEs and further test and improve the expanding flux rope model of CMEs by Chen et al. (1997). For this project we are using an extended sample of CMEs that were observed by both LASCO and EIT.

We are currently working on theoretical models of jet motion in the solar gravitational field which include the influence of a drag force. Our goal is to compare these models to the LASCO/EIT observations of a larger sample of polar jets, and try to better understand their kinematic behavior.

REFERENCES

- Acton, L. W., et al. 1992, PASJ, 44, L71
Chen, J. 1996, J. Geophys. Res., 101, 27499
Chen, J., et al. 1997, ApJ, 490, L191
Dere, K. P., & Mason, H. E. 1993, Sol. Phys., 144, 217
Karovska, M., Wood, B. E., Brueckner, G. E., Cook, J. W., & Howard, R. A. 1999a, in Solar Wind 9, ed. S. R. Habbal (New York: AIP), in press
Karovska, M., Wood, B. E., Cook, J. W., Howard, R. A., & Brueckner, G. E. 1999b, in SOHO 7 Workshop: Coronal Holes and Solar Wind Acceleration, ed. S. R. Cranmer & J. L. Kohl (Dordrecht: Kluwer), in press
Wang, Y.-M., et al. 1998, ApJ, 508, 899
Wood, B. E., Karovska, M., Brueckner, G. E., Chen, J., Cook, J. W., & Howard, R. A., 1998c, Eos Trans. AGU, 79, S268
Wood, B. E., Karovska, M., Chen, J., Brueckner, G. E., Cook, J. W., & Howard, R. A. 1999a, ApJ, to appear February 10
Wood, B. E., Karovska, M., Cook, J. W., Brueckner, G. E., & Howard, R. A. 1998a, BAAS, 29, 1321
Wood, B. E., Karovska, M., Cook, J. W., Brueckner, G. E., Howard, R. A., Korendyke, C. M., & Socker, D. G. 1998b, ApJ, 505, 432
Wood, B. E., Karovska, M., Cook, J. W., Howard, R. A., & Brueckner, G. E. 1999b, ApJ, submitted

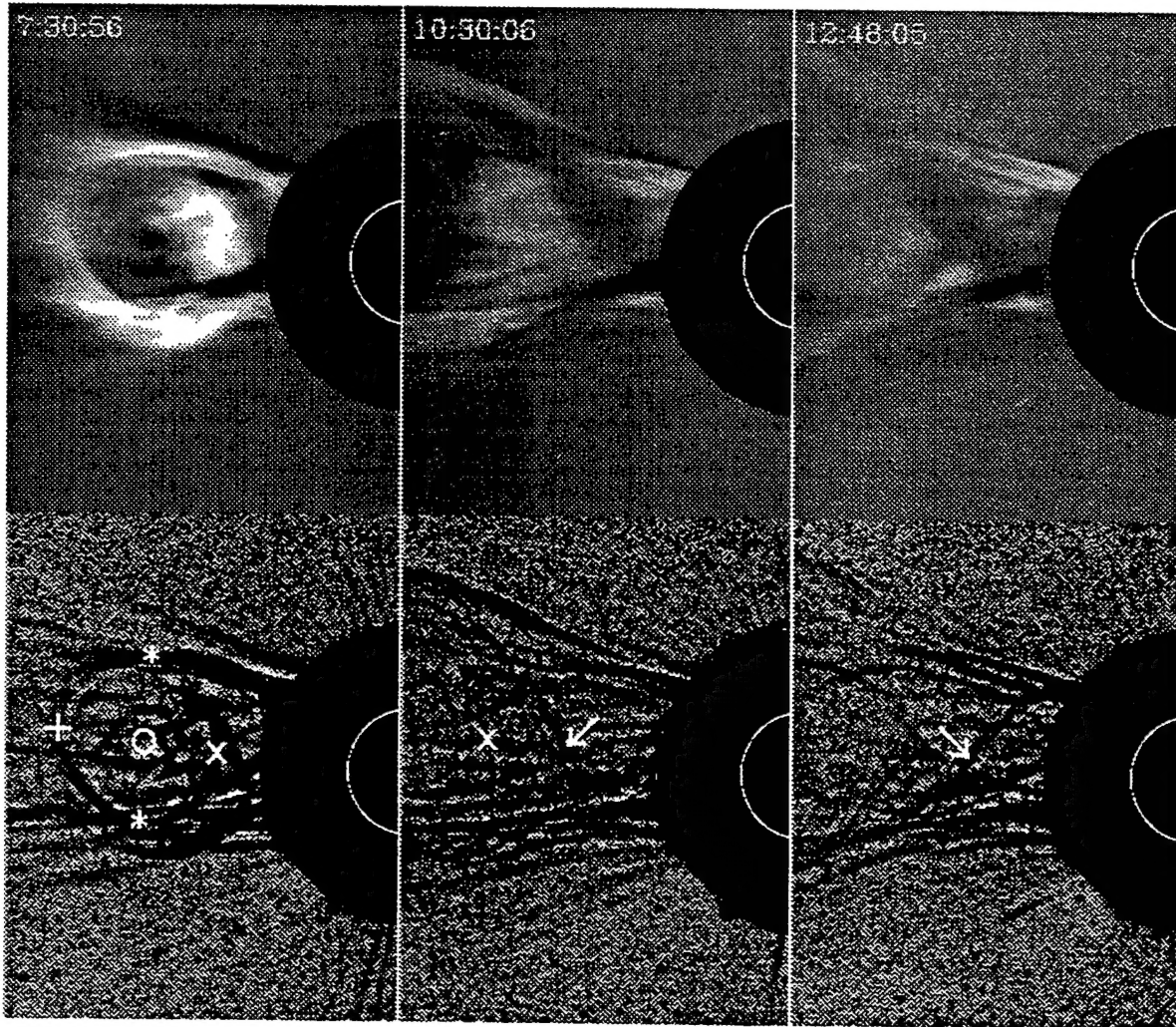


Figure 1: Average-differenced and edge-enhanced versions of three LASCO C2 images of the April 30 CME. The locations of the leading edge (plus sign), trailing edge (X's), sides (asterisks), and centroid (circle) of the bright circular rim structure of the CME are indicated. Helical lines are seen below the rim which possibly trace the magnetic field. Two of these lines are identified with arrows.

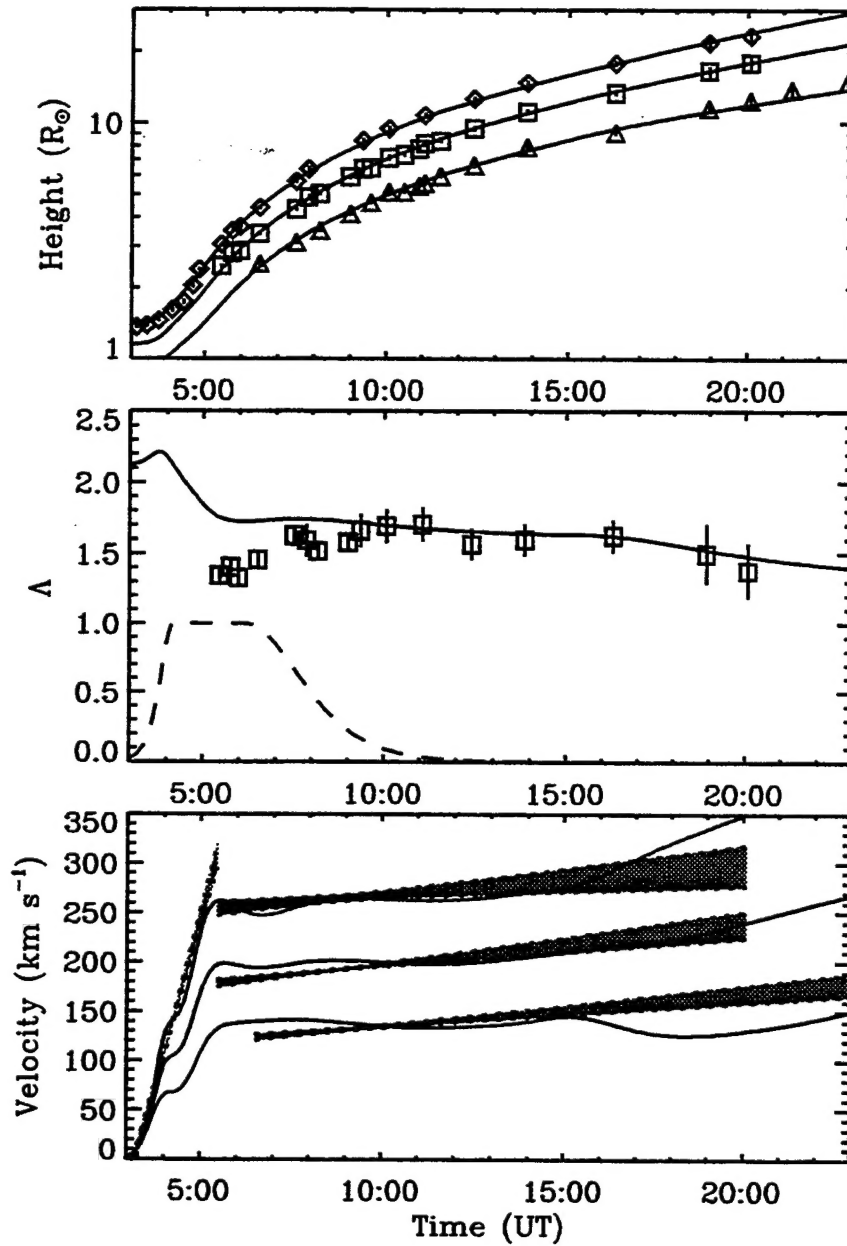


Figure 2: In the top panel, the height measurements for the leading edge (diamonds), centroid (boxes), and trailing edge (triangles) of the April 30 CME are plotted; and in the bottom panel our velocity measurements from these data are displayed (shaded regions). These measurements are compared with the theoretical predictions of an expanding flux rope model (solid lines). In the middle panel, both observed and model values for the aspect ratio Λ are plotted. Also shown is a normalized flux injection profile used in the flux rope model (dashed line).

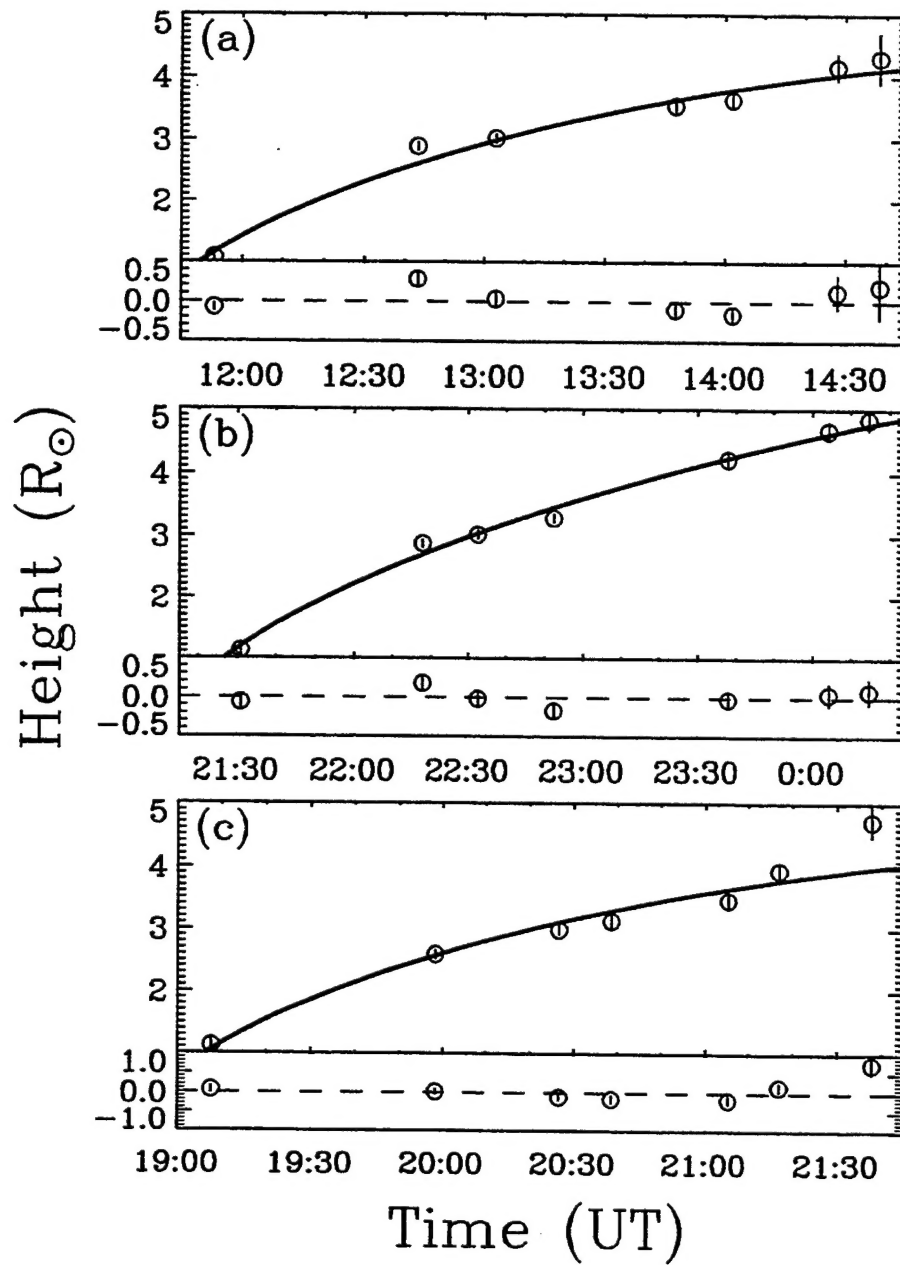


Figure 3: The centroids of three polar jets from 1997 August 5 (circles) measured using Gaussian fits to the intensity tracings obtained from LASCO C2 data. For each jet a single additional data point at heights below the C2 field of view is provided by EIT images. The centroid measurements are fitted with ballistic trajectories (solid lines), and residuals of the fit are displayed below the main figures.